

where  $\Gamma = 4\pi\eta L/[\ln(L/2R) + 0.84]$  is the Stokes drag coefficient for a cylinder (26), and  $\eta$  is the effective viscosity of the nematic. The solid lines in Fig. 4B are the results of fits to the solution of this equation

$$z(t) = \left( z_0 - \frac{\delta Mg}{4\pi KC(\partial\theta/\partial z)^2} \right) [1 - \exp(-t/\tau)] \quad (6)$$

with the time constant,  $\tau = \Gamma/[4\pi KC(\partial\theta/\partial z)^2]$ , constrained to have the same value,  $\tau = 270$  s, in all three fits. These results give clear qualitative support for Eqs. 4 to 6 in describing the levitation. Quantitative comparisons are made difficult by the complicated anisotropy of the nematic's viscoelasticity (21). However, selecting characteristic values for 5CB of  $\eta \sim 1$  Poise (27) and  $K \approx 5 \times 10^{-7}$  dynes leads to  $\tau \approx 140$  s, which is in reasonable agreement with the measured value.

This manipulation of wires with director gradients suggests methods for self-assembly using more elaborate spatially dependent director fields. For example, as a straightforward extension of the levitation, a liquid crystal that twists through many periods (such as a cholesteric liquid crystal) could serve as host to the creation of a periodic array of planes of oriented nano-

wires. Another possible application of these forces involves wire sorting through the repulsion from a flat surface. As Eq. 3 indicates, gravity and the repulsive force balance at a height that varies to first order with  $R^{-2}$  and is independent of  $L$  when  $\theta$  is fixed; for example, by a large external field. Hence this repulsion can be used to spatially separate wires of different radii.

#### References and Notes

- W. B. Russel, D. A. Saville, W. R. Schowalter, *Colloidal Dispersions* (Cambridge Univ. Press, Cambridge, 1989).
- F. C. MacKintosh, C. F. Schmidt, *Curr. Opin. Colloid Interface Sci.* **4**, 300 (1999).
- T. L. Morkved, P. Wiltzius, H. M. Jaeger, D. G. Grier, T. A. Witten, *Appl. Phys. Lett.* **64**, 422 (1994).
- R. B. Thompson, V. V. Ginzburg, M. W. Matsen, *Science* **292**, 2469 (2001).
- K. Shin *et al.*, *Nano Lett.* **2**, 933 (2002).
- N. Bowden, A. Terfort, J. Carbeck, G. M. Whitesides, *Science* **276**, 233 (1997).
- P. Poulin, H. Stark, T. C. Lubensky, D. A. Weitz, *Science* **275**, 1770 (1997).
- P. Poulin, V. Cabuil, D. A. Weitz, *Phys. Rev. Lett.* **79**, 4862 (1997).
- T. C. Lubensky, D. Pettey, N. Currier, H. Stark, *Phys. Rev. E* **57**, 610 (1998).
- O. Mondain-Monval, J. C. Dedieu, T. Gulik-Krzywicki, P. Poulin, *Eur. Phys. J. B* **12**, 167 (1999).
- J.-C. Loudet, P. Barois, P. Poulin, *Nature* **407**, 611 (2000).
- J. C. Loudet, P. Poulin, *Phys. Rev. Lett.* **87**, 165503 (2001).
- J.-I. Fukuda, B. I. Lev, K. M. Aoki, H. Yokoyama, *Phys. Rev. E* **66**, 051711 (2002).

- M. Tasinkevych, N. M. Silvestre, P. Patricio, M. M. Telo de Gama, *Eur. Phys. J. E* **9**, 341 (2002).
- F. Brochard, P. G. de Gennes, *J. Phys. (Paris)* **31**, 691 (1970).
- F. Alouges, B. D. Coleman, *J. Phys. A Math. Gen.* **32**, 1177 (1999).
- D. Andrienko, M. P. Allen, G. Skacej, S. Zumer, *Phys. Rev. E* **65**, 041702 (2002).
- A. B. Bracic, K. Kocevar, I. Musevic, S. Zumer, *Phys. Rev. E* **68**, 011708 (2003).
- The nickel wires were fabricated via electrodeposition into nanoporous alumina templates [M. Tanase *et al.*, *Nano Lett.* **1**, 155 (2001)].
- The sizes of the applied magnetic fields are several orders of magnitude smaller than those required to reorient the nematic director because of its magnetic anisotropy.
- P. G. de Gennes, J. Prost, *The Physics of Liquid Crystals* (Oxford Univ. Press, Oxford, 1993).
- This expression for the capacitance is for an ellipsoid and therefore is only approximate for the case of a cylinder.
- N. V. Madhusudana, R. Pratibha, *Mol. Cryst. Liq. Cryst.* **89**, 249 (1982).
- A. Hultgren, M. Tanase, C. S. Chen, G. J. Meyer, D. H. Reich, *J. Appl. Phys.* **43**, 7554 (2003).
- The height based on a superposition of two elastic forces is only an approximate solution. The exact solution requires solving the boundary value problem that accounts for all three surfaces (wire and two planes) simultaneously.
- M. M. Tirado, J. G. de la Torre, *J. Chem. Phys.* **71**, 2581 (1979).
- A. G. Chmielewski, *Mol. Cryst. Liq. Cryst.* **132**, 339 (1986).
- We thank C. Denniston and J. Harden for helpful discussions and M. Tanase for assistance with wire synthesis. Funding was provided by NSF through grants DMR-0134377 and DMR-0080031.

15 October 2003; accepted 11 December 2003

## Local Gate Control of a Carbon Nanotube Double Quantum Dot

N. Mason,\*† M. J. Biercuk,\* C. M. Marcus†

We have measured carbon nanotube quantum dots with multiple electrostatic gates and used the resulting enhanced control to investigate a nanotube double quantum dot. Transport measurements reveal honeycomb charge stability diagrams as a function of two nearly independent gate voltages. The device can be tuned from weak to strong interdot tunnel-coupling regimes, and the transparency of the leads can be controlled independently. We extract values of energy-level spacings, capacitances, and interaction energies for this system. This ability to control electron interactions in the quantum regime in a molecular conductor is important for applications such as quantum computation.

Carbon nanotubes have been considered leading candidates for nanoscale electronic applications (1, 2). Previous measurements of nanotube electronics have shown electron confinement (quantum dot) effects such as single-electron charging and energy-level quantization (3–5). Nanotube properties such as long spin lifetimes make them ideal candidates for spin-

based quantum computation based on double quantum dots (6) or multiple series quantum dots (7). However, realizing such devices requires independent gate control over multiple charges and spins. This ability has not been achieved in previous measurements, where device properties were controlled with a single global gate such as the doped silicon substrate (8–10). We report the fabrication and measurement of a nanotube-based double quantum dot with multiple, independent gates. The gates are used to manipulate and study single-electron charging as well as charge interactions, and relevant device parameters are extracted directly from transport data.

The device under study consists of a nanotube  $\sim 2$  nm in diameter, of length  $L \sim 1.5$   $\mu\text{m}$  between metal contacts, with three top gates (11, 12) and a doped Si backgate (Fig. 1) (13). Room temperature measurements of conductance as a function of any gate voltage indicate either that the nanotube is metallic with a strong resonance or that it is a small band-gap semiconductor. At low temperatures, single-electron charging is observed as Coulomb blockade conductance peaks, measured as a function of applied gate voltages. The observed peak pattern is different for each gate and in some regions shows considerable superstructure, which appears with increasing source-drain voltage,  $V_{SD}$ . We observe a double periodicity of Coulomb charging phenomena, which is consistent with a nanotube quantum dot, defined by tunnel barriers to the leads, that has been split into two dots of roughly equal size by a defect in the middle of the device (14). Structural defects often create tunable tunnel barriers (15–18) and typically appear in nanotubes longer than  $\sim 200$  nm. Although such defects can be controllably fabricated (19), in this case the defect is inherent to the tube. The resulting dots each have a quantized energy level spacing of  $\Delta = \hbar v_F/2L \sim 1$  meV (assuming only spin degeneracy), where  $v_F = 8.1 \times 10^5$  m/s is the Fermi velocity for a metallic nanotube (4).

The top gate voltages have differential capacitive coupling to the quantized energy levels of the two dots. Transport measurements indi-

Department of Physics, Harvard University Cambridge, MA 02138, USA.

\*These authors contributed equally to this work.  
†To whom correspondence should be addressed. E-mail: marcus@harvard.edu (C.M.M.); nmason@fas.harvard.edu (N.M.)

## REPORTS

cate that gate G1 predominantly couples to dot 1 and gate G2 to dot 2. In the transconductance,  $dI/dV_{G1}$ , as a function of  $V_{G1}$  and  $V_{G2}$  (Fig. 2A), paired regions of large  $dI/dV_{G1}$  appear on the vertices of a hexagonal lattice (13). The resulting honeycomb-shaped array of high  $dI/dV_{G1}$  can be contrasted with the straight lines that would appear if each applied gate voltage coupled equally to the dots. The observed pattern strongly resembles the charge stability diagram found for weakly tunneling double quantum dot (interdot tunneling  $\ll 2e^2/h$ ), where each cell of the honeycomb corresponds to a well-defined electron configuration for the double dot (20). The vertex pairs are points of degeneracy between the two dots that have split because of interdot coupling (either capacitive or tunneling). At these vertices, energy levels resonantly align between the dots as well as the leads (Fig. 2C). For a series double dot, resonant transport only occurs at the vertices; finite nonresonant conductance along the edges of the honeycomb cells (Fig. 2, D and E) occurs via cotunneling, which is suppressed in the weak-tunneling regime (20).

At finite bias, the vertex points expand into triangular regions (Fig. 2B) defined by lines where the energy levels of each dot align with either the top or bottom of the bias window. According to theory, resonant tunneling should occur only along the one side of the triangle that connects the original vertices. The observation of off-resonance tunneling in the body of the triangles has previously been attributed to both inelastic phonon contributions and cotunneling processes (21–23). Because it appears that cotunneling is suppressed in this region (we do not see conduction along the edges of the honeycomb), conduction inside the finite-bias triangles suggests, perhaps, a substantial contribution from electron-phonon coupling to trans-

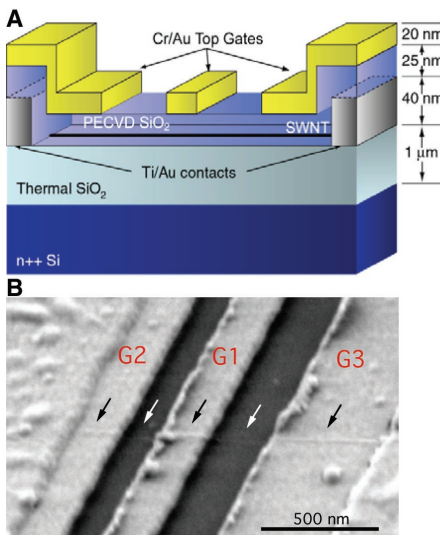


**Fig. 1.** (A) Schematic of top-gated device. (B) Electron micrograph of a representative device. Arrows indicate the embedded nanotube.

port. However, this conclusion appears inconsistent with the predicted suppression of electron-phonon coupling in nanotubes at low temperatures (24, 25). It seems more likely that inelastic processes are occurring through electron interactions with the source/drain reservoirs or the substrate. Figure 2B does not show resonant excited-state levels inside the finite-bias triangles, as are observed in lateral quantum dots (20). This is not surprising, as  $eV_{SD} < \Delta$  in the present case. Increasing  $V_{SD}$  causes the triangles to grow, as expected, but also inhibits our ability to resolve individual vertices and even individual honeycomb cells. Overall, however, the transport characteristics of this nanotube double dot are qualitatively similar to those observed for double dots fabricated in semiconductor heterostructures (21, 26). Such similarities suggest that more complex quantum devices formed from molecular conductors such as nanotubes will continue to share features with well-studied semiconductor quantum dot systems. However, the larger energy scales in carbon nanotubes allow operation at higher temperatures.

Double dot capacitances are obtained by measuring the sizes and separations of the honeycombs and vertices (Fig. 2) (20). The size of the honeycomb in Fig. 2A determines  $\Delta V_{G1(2)}$ , where

$$\Delta V_{G1(2)} = \frac{|e|}{C_{G1(2)}} (1 + \Delta/E_{C1(2)}) \quad (1)$$

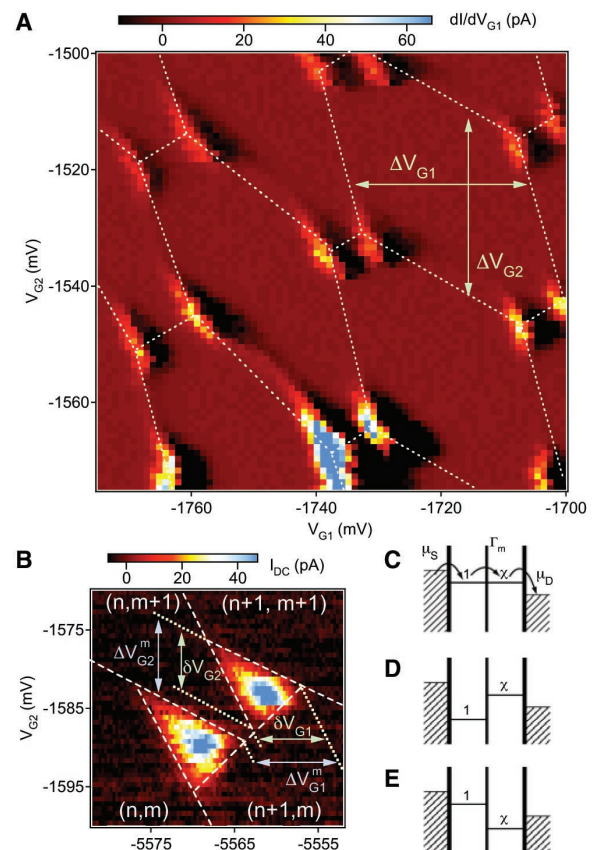
with  $C_{G1(2)}$  the capacitance of dot 1(2) to gate 1(2) and  $E_{C1(2)} \sim 2\text{meV}$  the charging energy for dot 1(2).  $E_{C1(2)}$  is determined from  $|eV_{SD}|$  measured at the apex of a conductance diamond in a plot of conductance as a function of  $V_{SD}$  and any gate voltage (not shown). From the size of the finite-bias triangles in Fig. 2B, we determine capacitance ratios using

$$\delta V_{G1(2)} = \frac{C_{1(2)}}{C_{G1(2)}} V_{SD} \quad (2)$$

With the above relationships, we calculate typical dot capacitances of  $C_{1(2)} \sim 160$  aF and  $C_{G1(2)} \sim 45$  aF.

The amount of capacitive coupling and interdot tunneling can be determined from the vertex splitting (27, 28). These couplings cause an energy shift related to the formation of charge polarized, or “bonding,” states between the quantum dots (tunnel coupling is analogous to covalent bonding, and capacitive coupling to ionic bonding). Both coupling parameters can be tuned with gate voltages that open the interdot constriction, so it is difficult to determine their relative contributions to

**Fig. 2.** Experimental charge stability diagrams for the series double quantum dot as a function of two gate voltages, each shifting the energy levels of a single dot. Voltages  $V_{G1}$  and  $V_{G2}$  are divided by five before being applied to the gates of the device. (A) Color scale displays  $dI/dV_{G1}$  calculated from dc current ( $I_{DC}$ ) at  $V_{SD} = 500 \mu\text{V}$ . White lines are guides to the eye showing the honeycomb pattern of peaks in conductance. Vertex pairs correspond to points of degeneracy between the two dots where resonant transport occurs, whereas cotunneling may produce finite conductance along the honeycomb edges. (B) Zoom-in of a vertex pair at  $V_{SD} = 500 \mu\text{V}$  with lines of constant energy designated by white dashed lines. Colorscale displays  $I_{DC}$ . Vertex dimensions are indicated on the diagram, as are particular electron configurations on the two dots for different regions of gate space. Note the triangular shape resulting from finite  $V_{SD}$ , and nonzero off-resonance conductance within the triangles. (C) Level diagrams for a double quantum dot depicting resonant transport with  $\Gamma_m^m$  the interdot tunnel rate. The bias window is  $V_{SD} = (\mu_S - \mu_D)/e$ . (D and E) Level diagrams depicting configurations where cotunneling may contribute to transport.



vertex splitting. If we assume the vertex splitting is due to capacitive coupling alone, we find a mutual capacitance between dots  $C_m \sim 90$  aF, using

$$\Delta V_{G_{1(2)}}^m = \frac{|e|C_m}{C_{G_{1(2)}}C_{2(1)}} \quad (3)$$

where  $\Delta V_{G_{1(2)}}^m$  is the horizontal or vertical component of the diagonal splitting measured between vertices (20). A separate determination of the mutual capacitance based on single-dot capacitances (determined above) and the magnitude of the charging energy using the relation

$$E_{C_{1(2)}} = \frac{e^2}{C_{1(2)}} (1 - C_m^2/C_1C_2)^{-1} \quad (4)$$

gives  $C_m \sim 100$  aF. The similarity between these two values for  $C_m$  indicates that the vertex splitting in this region is dominated by capacitive coupling. The interaction energy is then approximately

$$E_m = \frac{e^2}{C_m} (C_1C_2/C_m^2 - 1)^{-1} \sim 700 \mu\text{eV}. \quad (5)$$

Opening the interdot constriction is expected to increase the tunnel coupling exponentially faster than the capacitive coupling (27). We can therefore compare the amount of interdot tunnel coupling in different gate configurations using the fractional peak splitting, defined  $f = 2\Delta V_S/\Delta V_P$  where  $\Delta V_S$  is the diagonal splitting measured between vertices

and  $\Delta V_P$  is the distance between vertex pairs (Fig. 3A) (26). A value of  $f = 1$  corresponds to a transparent interdot constriction, while  $f = 0$  indicates two isolated dots in the limit of zero mutual capacitance between dots. Changes in  $f$ , however, should be dominated by tunnel coupling, so measuring how  $f$  changes as a function of gate voltage allows the contribution to the vertex splitting from interdot tunneling to be inferred. We observe an evolution of  $f$  by holding the range of  $V_{G2}$  fixed and examining different regimes of  $V_{G1}$  (Fig. 3, A and B). In Fig. 3A, where honeycomb cells and vertices are well defined, we find that  $f \sim 0.3$ . This regime can be contrasted with that of Fig. 3B, where an increase in interdot tunnel coupling leads to a smearing of vertices and honeycomb cells. In this region, vertex splitting grows to a value of  $f \sim 0.7$ .

In Fig. 3, C to E, we use a combination of  $V_{G1}$  and  $V_{G2}$  to maintain a fixed electron configuration while tuning tunneling with the backgate. The evolution evident here shows how varying  $V_{BG}$  from 250 mV to 375 mV changes our stability diagram from weak to strong cotunneling regimes. The corresponding increase in vertex heights indicates that we are also influencing the total amount of tunneling through the double dot. Because the vertex splitting does not change substantially, it seems that the backgate is primarily tuning the transparency of the tunnel barriers at the source and/or drain electrodes (15).

Increasing temperature increases cotunneling conductance (i.e., conductance on honeycomb edges) by a relation well described by a power law,  $G_{cot} \propto T^\eta$ , over the range investigated, where  $\eta$  is between 1 and 2 with a typical value of  $\eta \sim 1.3$  (Fig. 4, A and C, upper curve). In contrast, resonant vertex peak conductance is roughly independent of temperature, or only slightly increases with increasing temperature (Fig. 4, B and C, lower curve). Power law behavior with  $\eta = 2$  has been predicted for cotunneling peaks in the weak interdot tunneling regime ( $G_{int} \ll e^2/h$ ) at low temperatures ( $k_B T \ll \Delta$ ) (29). A power law with  $\eta = 1.25$ —comparable to what we find—is predicted (29) for intermediate tunnel coupling, and  $\Delta \ll k_B T$  (corresponding to temperatures higher than those of our measurements). The nearly temperature-independent behavior we observe for resonant peaks does not appear consistent with predictions of peak height scaling as  $1/T$  in the low-temperature regime (28, 30). Given that other measurements of this system correspond relatively well to predicted behavior, it is surprising that the temperature dependence deviates so far from theoretical expectations.

**Fig. 3.** (A) Experimental charge stability diagram demonstrating weak interdot tunnel coupling,  $V_{SD} = 500 \mu\text{V}$ . Vertex peak splitting ( $\Delta V_S$ ) and honeycomb cell dimensions ( $\Delta V_P$ ) indicated on the plot. (B) Moving to a different region of  $V_{G1}$  changes the tunnel coupling between dots, producing a smeared charge stability diagram. (C to E) Experimental stability diagrams for fixed charge configuration at various  $V_{BG}$ .  $V_{SD} = 800 \mu\text{V}$ . The capacitive coupling of the backgate to the two dots requires that slightly different ranges of  $V_{G1}$  and  $V_{G2}$  be used to cover the same charge configurations at different  $V_{BG}$  values.

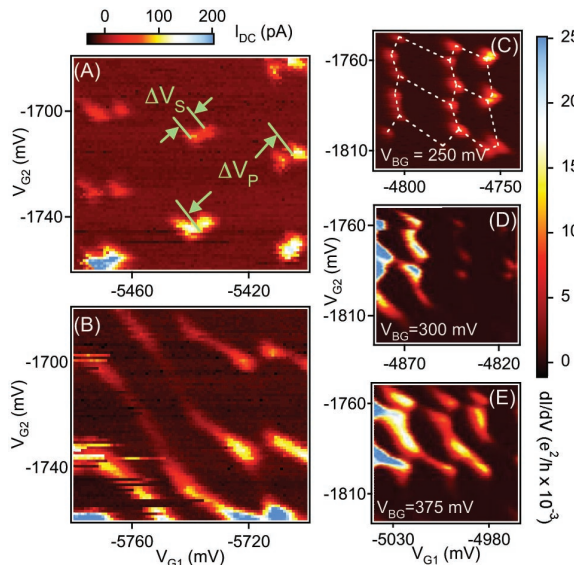
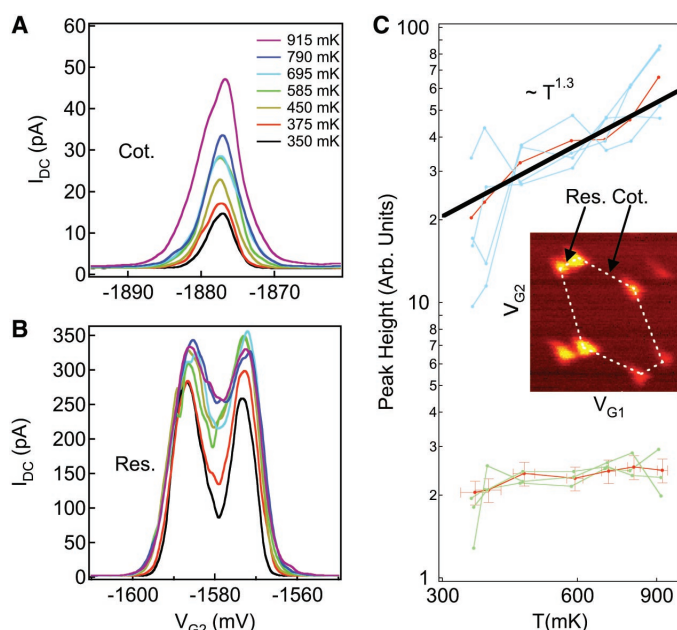


**Fig. 4.** Temperature dependence of peak heights for two different regimes of transport. One-dimensional sweeps taken in  $V_{G2}$  with  $V_{G1} = -1800$  mV. Representative cotunneling peak (A), denoted "Cot.," and vertex peaks (B), denoted "Res.," at temperatures between  $T = 350$  mK and 915 mK. (C) Peak height as a function of temperature on a log-log plot. Peaks are sorted by type (resonant or cotunneling) into two distinct groups and have all been offset to collapse approximately onto a single curve for each group. The black line shows the average power law behavior,  $T^{1.3}$ , for cotunneling peaks. Peaks shown in (A) and (B) are shown in red. (Inset) Representative honeycomb cell in the region of measurement.



#### References and Notes

1. C. Dekker, *Phys. Today* **52**, 22 (1999).
2. T. W. Odom, J. L. Huang, P. Kim, C. M. Lieber, *J. Phys. Chem. B* **104**, 2794 (2000).

3. S. J. Tans *et al.*, *Nature* **386**, 474 (1997).
4. M. Bockrath *et al.*, *Science* **275**, 1922 (1997).
5. J. Kong, C. W. Zhou, E. Yenilmez, H. J. Dai, *Appl. Phys. Lett.* **77**, 3977 (2000).
6. D. Loss, D. P. DiVincenzo, *Phys. Rev. A* **57**, 120 (1998).
7. D. P. DiVincenzo, D. Bacon, J. Kempe, G. Burkard, K. B. Whaley, *Nature* **408**, 339 (2000).
8. Multiple quantum dots without independent control have been observed previously in carbon nanotubes. See (10) and (17).
9. K. Ishibashi, M. Suzuki, T. Ida, Y. Aoyagi, *Appl. Phys. Lett.* **79**, 1864 (2001).
10. J. Lefebvre, J. F. Lynch, M. Llaguno, M. Radosavljevic, A. T. Johnson, *Appl. Phys. Lett.* **75**, 3014 (1999).
11. M. J. Biercuk, N. Mason, C. M. Marcus, *Nano Lett.*, in press, published online 19 November 2003.
12. S. J. Wind, J. Appenzeller, P. Avouris, *Appl. Phys. Lett.* **80**, 3817 (2002).
13. Materials and methods are available as supporting material on Science Online.
14. Measurements of conductance as a function of bias voltage and gate voltage show Coulomb blockade with two nearly equivalent charging energies, indicating that the two dots are of equal size. The symmetry of the honeycombs in Fig. 2 also indicates that the charging energies of the two dots are nearly equal.
15. M. Bockrath *et al.*, *Science* **291**, 283 (2001).
16. L. Chico, L. X. Benedict, S. G. Louie, M. L. Cohen, *Phys. Rev. B* **54**, 2600 (1996).
17. T. Kostyrko, M. Bartkowiak, G. D. Mahan, *Phys. Rev. B* **59**, 3241 (1999).
18. H. J. Choi, J. Ihm, S. G. Louis, M. L. Cohen, *Phys. Rev. Lett.* **84**, 2917 (2000).
19. M. J. Biercuk, N. Mason, J. Chow, C. M. Marcus, available at <http://arXiv.org/abs/cond-mat/0312276>.
20. W. G. van der Wiel *et al.*, *Rev. Mod. Phys.* **75**, 1 (2003).
21. N. C. van der Vaart *et al.*, *Phys. Rev. Lett.* **74**, 4702 (1995).
22. T. Fujisawa *et al.*, *Science* **282**, 932 (1998).
23. D. V. Averin Yu, V. Nazarov, in *Single Charge Tunneling: Coulomb Blockade Phenomena in Nanostructures*, H. Grabert, M. H. Devoret, Eds. (Plenum Press and NATO Scientific Affairs Division, New York/London, 1992).
24. J. Hone, B. Batlogg, Z. Benes, A. T. Johnson, J. E. Fischer, *Science* **289**, 1730 (2000).
25. J. Vavro *et al.*, *Phys. Rev. Lett.* **90**, 65503 (2003).
26. C. Livermore, C. H. Crouch, R. M. Westervelt, K. L. Campman, A. C. Gossard, *Science* **274**, 1332 (1996).
27. L. P. Kouwenhoven *et al.*, in *Mesoscopic Electron*

- Transport*, L. P. Kouwenhoven, G. Schön, L. L. Sohn, Eds. (Kluwer, Dordrecht, Netherlands, 1997).
28. A. Kaminski, L. I. Glazman, *Phys. Rev. B* **59**, 9798 (1999).
29. K. A. Matveev, L. I. Glazman, H. U. Baranger, *Phys. Rev. B* **54**, 5637 (1996).
30.  $1/T$  behavior is expected for  $\Gamma < k_B T \ll \Delta$ .
31. The authors wish to thank J. Hone, A. C. Johnson, and J. B. Miller for useful discussions, and H. Park for assistance with the design of the nanotube chemical vapor deposition system. This work was supported by funding from the NSF through the Harvard Materials Research Science and Engineering Center, the NSF under EIA-0210737, and the Army Research Office/Advanced Research and Development Authority Quantum Computing Program. N.M. acknowledges support from the Harvard Society of Fellows. M.J.B. acknowledges support from an NSF Graduate Research Fellowship and from an ARO Quantum Computing Graduate Research Fellowship.

**Supporting Online Material**

[www.sciencemag.org/cgi/content/full/303/5658/655/DC1](http://www.sciencemag.org/cgi/content/full/303/5658/655/DC1)

Materials and Methods

13 November 2003; accepted 24 December 2003

# An ab Initio Molecular Dynamics Study of the Aqueous Liquid-Vapor Interface

I-Feng W. Kuo and Christopher J. Mundy\*

We present an ab initio molecular dynamics simulation of the aqueous liquid-vapor interface. Having successfully stabilized a region of bulk water in the center of a water slab, we were able to reproduce and further quantify the experimentally observed abundance of surface “acceptor-only” (19%) and “single-donor” (66%) moieties as well as substantial surface relaxation approaching the liquid-vapor interface. Examination of the orientational dynamics points to a faster relaxation in the interfacial region. Furthermore, the average value of the dipole decreases and the average value of the highest occupied molecular orbital for each water molecule increases approaching the liquid-vapor interface. Our results support the idea that the surface contains, on average, far more reactive states than the bulk.

Although the nature of bulk liquid water itself remains incompletely understood, there is a more pressing need to characterize water in more complex environments. In particular, the interfaces between liquid water and hydrophobic material or air engender important phenomena in biology (1–5) and atmospheric science (6, 7), respectively. These two interfaces seem to have much in common (1), and both are currently the subject of intense scrutiny.

Experimentalists have led the way in characterizing the aqueous liquid-vapor interface. Measurements of the aqueous liquid-vapor interface have provided proof of dangling OH bonds present at the surface (8, 9). Recent x-ray experiments on the aqueous liquid-vapor inter-

face have provided strong evidence for surface relaxation (10) and for new structural moieties in which both hydrogens (called “acceptor-only”) of a surface water molecule are dangling (11, 12). To date, theoretical models have not captured all these surface phenomena, presumably because the models were fitted to reproduce properties of the homogeneous bulk phases. Ab initio simulations lend themselves well to these studies because they present an unbiased representation of water in different environments and are thus ideal candidates for elucidating surface phenomena. Here, we used Car-Parinello molecular dynamics (CPMD) (13, 14) to investigate the properties of the aqueous liquid-vapor interface (15, 16).

The shortest distance from the aqueous liquid-vapor interface at which one can observe bulk liquid behavior is  $\sim 10 \text{ \AA}$  (17). Due to the computational demands of ab initio methods, we needed to determine the smallest system one can simulate that will produce a stable interface. A

recent ab initio study of the aqueous liquid-vapor interface using 32 waters produced interesting results regarding dangling bonds but

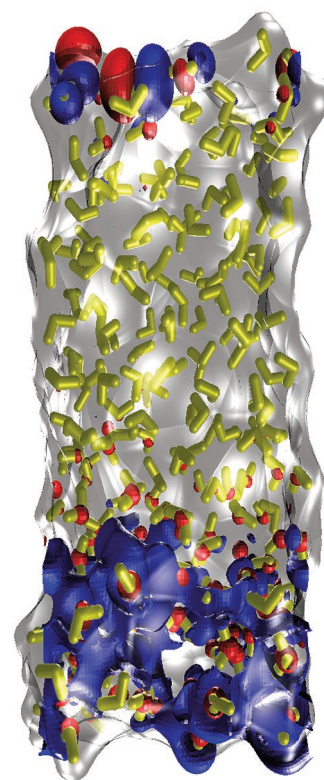


**Fig. 1.** Snapshot of the calculated aqueous liquid-vapor interface. The individual water monomers are represented by yellow cylinders. The colored isosurfaces on the top represent the HOMO, whereas the colored isosurfaces at the bottom represent the LUMO. The orbitals are obtained by direct diagonalization of the KS matrix, indicating that the reactivity of the water slab is localized on the surface for protons and electrons.

Computational Chemical Biology, Chemistry and Materials Science L-091, Lawrence Livermore National Laboratory, Livermore, CA 94550, USA.

\*To whom correspondence should be addressed. E-mail: [mundy2@llnl.gov](mailto:mundy2@llnl.gov)